Neural Comput & Applic (2013) 23:2281–2293
DOI 10.1007/s00521-012-1179-8

ORIGINAL ARTICLE

Efficient sparse unmixing analysis for hyperspectral imagery based on random projection

Zhenwei Shi · Liu Liu · Xinya Zhai · Zhiguo Jiang

Received: 28 June 2012 / Accepted: 11 September 2012 / Published online: 25 September 2012

Abstract Hyperspectral imagery including rich spectral information could be applied to detect and identify objects at a distance. In this paper, we concentrate on the surface material identification of interested objects within the domain of space object identification (SOI) and geological survey. One of the approaches is the unmixing analysis that identifies the components (called endmembers) in each pixel and estimates their corresponding fractional abundances, and then, we could obtain the space distributions of substances. To solve this problem, we present an approach in a semi-supervised fashion, by assuming that the measured spectrum is expressed in the form of linear combination of a number of pure spectral signatures in a spectral library and the fractional abundances are their weights. Thus, the abundances are sparse and we propose a sparse regression model to realize the sparse unmixing analysis. We apply random projection technique to accelerate the sparse unmixing process and use split Bregman iteration to optimize the objective function. Our algorithm is tested and compared with other classic algorithms by using simulated hyperspectral images and a real-world image.

Keywords Hyperspectral image · Sparsity unmixing · Random projection

Z. Shi (✉) · L. Liu · X. Zhai · Z. Jiang
Image Processing Center, School of Astronautics, Beihang University, Beijing 100191, People's Republic of China
e-mail: shizhenwei@buaa.edu.cn

L. Liu
e-mail: liuliubh@gmail.com

X. Zhai
e-mail: zhaixinya_1750@yahoo.com.cn

Z. Jiang
e-mail: jiangzg@buaa.edu.cn

Z. Shi
Beijing Key Laboratory of Digital Media, Beihang University, Beijing 100191, People's Republic of China

Z. Shi
State Key Laboratory of Virtual Reality Technology and Systems, Beihang University, Beijing 100191, People's Republic of China

1 Introduction

Hyperspectral imagery could be regarded as a stack of images. Each pixel is represented by a spectral signature that characterizes the underlying objects. It can be used in many application domains, for example, monitoring environmental and urban processes or risk prevention and response. This paper concentrates on the surface material identification of interested objects, namely to obtain their structure information within the domain of space object identification (SOI) and geological survey. However, if the spatial resolution of the imaging sensor is not high enough to separate different materials, these can jointly occupy a single pixel. It becomes an obstacle to material identification according to the spectral fingerprints.

To deal with this problem, spectral mixture analysis techniques identify a collection of spectrally pure constituent spectra, called endmembers and estimate the fractions or abundances that indicate the proportion of each endmember presented in the pixel [1]. Some classical techniques for this purpose assume that the hyperspectral image contains at least one pure pixel for each endmember in the scene and extracts the endmembers first and estimates the fractions then. We can list some popular approaches [2] such as the pixel purity index (PPI) [3], N-FINDR [4], orthogonal subspace projection (OSP) technique [5], and

vertex component analysis (VCA) [6]. However, the unmixing results could not be accurate under the assumption because of the inadequate spatial resolution and the microscopic mixture of distinct materials [7]. Other unsupervised methods such as nonnegative matrix factorization (NMF) [8, 9] decompose the input data matrix into the endmember matrix and fractional matrix. It needs to make sure the number of endmembers in advance and to identify what materials they are by comparing with the pure spectral signatures in the spectral library.

The algorithms mentioned above have the same problem of the inaccuracy of the solved endmembers in the endmember identification. With the improvement of the hyperspectral database, a semi-supervised approach based on a spectral library draws many scholars' attention. That is the sparse unmixing technique that takes all the pure spectral signatures in the library as pseudo-endmembers and estimates all the corresponding abundances and selects the true endmembers automatically according to their fractions. The sparsity is reflected in the fact that a mixed pixel in the scene contains a few pure substances, and yet the mixed pixel is estimated with too many pure substances in the library. With the sparse regularization, it obtains a sparse solution of abundances. In this paper, we propose the sparse unmixing model expressed in the form of matrices. To save the storage of memory and accelerate the computing, we adopt the random projection method to lower the dimension of the hyperspectral image and hyperspectral library. In order to find an optimal matrix solution, we use split Bregman iteration to optimize the sparse unmixing process.

The structure of the paper is as follows: in Sect. 2, we establish the sparse unmixing model and get a compressed version with the random projection technique in Sect. 3. In Sect. 4, we solve the sparse unmixing problem with the method of the split Bregman iteration. At last, we test our algorithm using some simulated hyperspectral images of space objects in Sect. 5 and end with the conclusion in Sect. 6.

2 Hyperspectral sparse unmixing model

Many algorithms use a linear mixing model to solve the unmixing problem. It corresponds to a reasonable balance between accuracy and model complexity. It assumes that the spectral response of a pixel in any given spectral band is a linear combination of all of the endmembers present in the pixel at the respective spectral band. For each pixel, it can be expressed as follows:

$$v_j = \sum_{i=1}^{P} h_{ij} s_i + n = Sh_j + n \tag{1}$$

where v_j is an L-dimension spectral vector of the jth pixel, L is the number of spectral bands, P is the number of endmembers, h_{ij} is the fractional abundance of the ith endmember of the jth pixel, w_i is an L-dimension spectral vector of the ith endmember, and n is an L-dimension vector collecting the errors affecting the measurements at each spectral band. $S = [s_1, s_2, \ldots, s_P]$ is an endmember matrix, and $h_j = [h_{1j}, h_{2j}, \ldots, h_{Pj}]^T$ is a vector of abundance.

Hyperspectral imagery is a 3D datacube, with two dimensions representing the spatial plane and one dimension representing the spectral band. We change the two-dimension spatial plane into a line. Thus, the hyperspectral imagery is a 2D matrix. The linear mixing model in the form of matrix is:

$$V = SH \tag{2}$$

where S is a $L \times Q$ spectral matrix collecting the pure spectral signatures from a spectral library, and H is a $Q \times K$ abundance matrix. Q is the total number of spectrums in the spectral library, $Q > P$ and $Q \gg L$. Thus, it has many solutions of H as it is an underdetermined system. Because the number of pure materials in each pixel is much less than in the spectral library, H is sparse. We can obtain a sparse unique solution using an efficient sparse regression technique. A very simple and intuitive measure of sparsity of H is the l_0 norm $\|H\|_0$ which denotes the number of nonzero components of the matrix. The sparse unmixing problem is:

$$(P_0) \qquad \min_H \|H\|_0 \qquad \text{s.t.} \quad V = SH \tag{3}$$

The problem (p_1) is NP hard. Contrary to it, the problem (p_1) is convex and it can be written as a linear programming (LP) problem. In the given circumstances related to matrix S, the problem (p_0) has the same solution as the problem (p_1) introduced by [10]. The following model by using Lagrange multipliers as:

$$(P_1) \qquad \min_H \frac{1}{2}\|V - SH\|_2^2 + \lambda\|H\|_1 \tag{4}$$

It is a l_1 minimization problem and could be solved by some standard convex optimal algorithms.

3 Random projection

Because of high dimensions of hyperspectral data, it causes too much computing consuming on both the storage of memory and computing time. Here we compress the original data with random projection [10–12] which has been widely used in machine learning [13, 14]. One advantage is that it reduces the dimensions of spectrums without knowing the characteristics bands of different substances in advance. It will save much computing consuming when we continue the unmixing process with the compressed hyperspectral images and hyperspectral library. Another

advantage of random projection is that it could preserve the Euclidean distance of estimation error in the objective function according to the following theorem.

Theorem 1 [10] *Let $R = (r_{ij})$ be a random $k \times d$ matrix, such that each entry r_{ij} is chosen independently according to N(0,1). For any vector fixed $u \in \mathbb{R}^d$ and any $0 < \epsilon < 1$, let $\hat{u} = \hat{R}u = \frac{1}{\sqrt{k}}Ru$. Then, $E(\|\hat{u}\|^2) = \|u\|^2$ and with the probability of at least $1 - e^{-(\epsilon^2-\epsilon^3)\frac{k}{4}}$*

$$|\|\hat{u}\|^2 - \|u\|^2| \le \epsilon\|u\|^2 \tag{5}$$

Applying Theorem 1, certain types of random matrices P, the pairwise Euclidean distances are preserved:

$$(1-\varepsilon)\|y_i - y_j\|^2 \le \|x_i - x_j\| \le (1-\varepsilon)\|y_i - y_j\| \tag{6}$$

for some $\varepsilon > 0$, where $y_i = Px_i$ and $y_j = Px_j$. These matrices include matrices whose entries are i.i.d random variable following a Gaussian or Bernoulli distribution, and partial orthonormal matrices. Besides these dense matrices, sparse matrices have been proposed with fast implementation. Put the matrix V and SH into Eq. (4), we get the compressed version of the objective function:

$$\min_H \frac{1}{2}\|R_dV - R_dSH\|_2^2 + \lambda\|H\|_1 \tag{7}$$

where R_d is a normal random matrix with size $d \times L$. d is the projected dimension. Due to $d < L$, dimensions of both R_dV and R_dS are lower than the original data V and S which are replaced in the sparse unmixed process. Thus, it saves storage memory and computing time.

Algorithm 1 Sparse unmixing analysis based on random projection (SUARP)

Step 1: Initialize random matrix R_d, construct the projected matrixes;

$$S_d = R_dS, \quad V_d = R_dV$$

Step 2: Initialize matrixes $H = B = D = 0$, $V_D = V_d$, and regularization parameters λ, μ, η;

Step 3: Update H, B, D, V_d alternately as follows:

$$H^{k+1} = (\mu S_d^T S_d + I)^{-1}(\mu S_d^T V_d^k - B^k + D^k),$$
$$D^{k+1} = \max(H^{k+1} + B^k - \lambda, 0),$$
$$B^{k+1} = B^k + H^{k+1} - D^{k+1},$$
$$V_D^{k+1} = V_D^k + V_d - S_dH^{k+1}.$$

Step 4: Continue the iterations in Step 3 until satisfying the convergence condition:

$$\frac{\|H^{k+1} - H^k\|_2}{\|H^k\|_2} \le tol, \quad tol \in R^+.$$

Step 5: Output H and find the indexes of rows that $H \ge \eta$. It is the index of endmembers in

the spectral library matrix S. Output the endmembers and their corresponding abundance

maps.

4 Split Bregman iteration

We use the split Bregman iteration to optimize the sparse unmixing model expressed in the form of matric. The split Bregman iteration algorithm was first introduced by Goldstein and Osher for solving total variation (TV), compressed sensing and other regularized problems [15]. It converges quickly when it is applied to the l_1-regularization problem, and its value of regularization parameter is constant. It solves a general optimization problem:

$$\arg\min_r |\phi(r)| + H(r) \tag{8}$$

where arg min means the solution of the objective function. $\phi(r)$ and $H(r)$ are both convex and $H(r)$ is differential. We make such two substitutions $t = \phi(r)$ and $E(r, t) = |t| + H(r)$. Then, we get the following optimization problem that is equivalent to Eq. (9):

$$\arg\min_{r,t} E(r,t) + \frac{\lambda}{2}\|t - \phi(r)\|_2^2 \tag{9}$$

where λ is a positive constant.

The main process using the split Bregman iteration is shown as follows:

$$p_r^{k+1} = p_r^k - \lambda(\nabla\phi)^T[\phi(r^{k+1}) - t^{k+1}] \tag{10}$$

$$p_t^{k+1} = p_t^k - \lambda[t^{k+1} - \phi(r^{k+1})] \tag{11}$$

where p_r^k and p_t^k represent the sub-differential of $E(r,t) + \frac{\lambda}{2}\|t - \phi(r)\|^2$. The iterations (11) and (12) are equivalent to the following:

$$(r^{k+1}, t^{k+1}) = \arg\min_{r,t} |t| + H(r) + \frac{\lambda}{2}\|t - \phi(r) + b^k\|_2^2, \tag{12}$$

$$b^{k+1} = b^k + [\phi(r^{k+1}) - t^{k+1}] \tag{13}$$

where b^k is a parameter that assists in the process of solving the extreme value.

We apply the iterations to solve the objective function, and then, Eq. (7) becomes as follows:

$$\min_{H,D} \frac{1}{2}\|R_dV - R_dSH\|_2^2 + \lambda\|D\|_1 \quad \text{s.t.} \quad D = H \tag{14}$$

Convert it into an unconstrained problem:

$$\min_{H,D} \lambda\|D\|_1 + \frac{\mu}{2}\|R_dV - R_dSH\|_2^2 + \frac{1}{2}\|D - H\|_2^2 \tag{15}$$

The regularization parameters λ and μ work as penalties balancing the energy functions. The optimization problem above is performed in an alternating fashion:

$$H^{k+1} = \arg\min \frac{\mu}{2}\|R_dV - R_dSH\|_2^2 + \frac{1}{2}\|D^k - H - B^{k+1}\|_2^2 \tag{16}$$

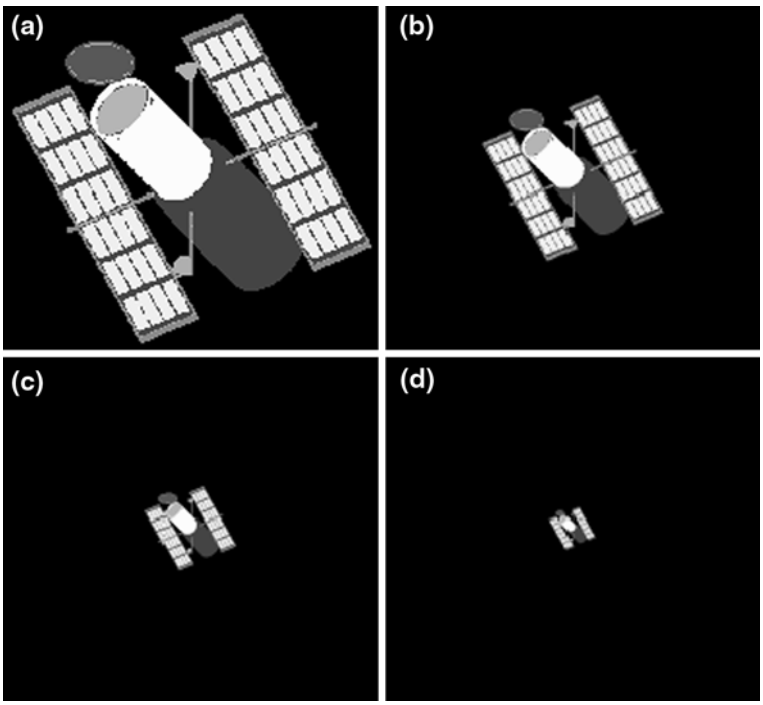

Fig. 1 Four simulated hyperspectral images with different space resolutions

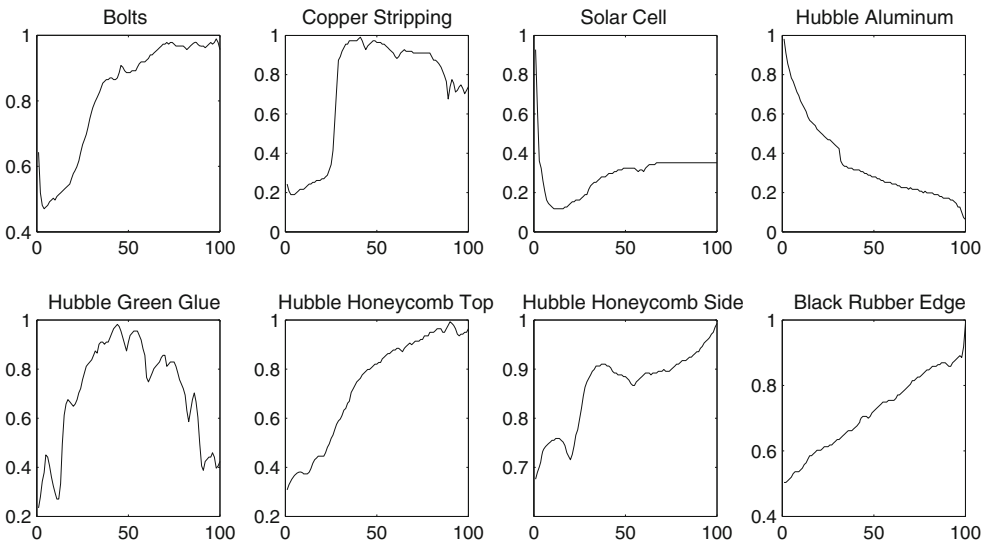

Fig. 2 Eight endmembers designed in the simulated data

$$D^{k+1} = \arg\min \lambda \|D\|_1 + \frac{1}{2}\|D - H^{k+1} - B^{k+1}\|_2^2 \quad (17)$$

$$B^{k+1} = B^k + H^{k+1} - D^{k+1} \quad (18)$$

where k denotes the iteration step.

In this fashion, we split the l_1 and l_2 components of minimization function. In the iteration process, we add an auxiliary variable V_D to accelerate the computing process. For more details, please refer to reference [15].

Algorithm 1 summarizes the basic procedure of our proposed algorithm (called SUARP).

5 Experimental results

A set of simulated images and a real image were applied to the following experiments. The simulated ones were used to analyze the performance of the proposed algorithm in detail. One of them was used to compare the proposed algorithm (called SUARP) with some other classical algorithms, which contained the split Bregman algorithm (called SB) [15], the OMP (orthogonal matching pursuit) [16], and basis pursuit algorithms (called BP) [17]. Because the accurate solutions of the simulated data were known in

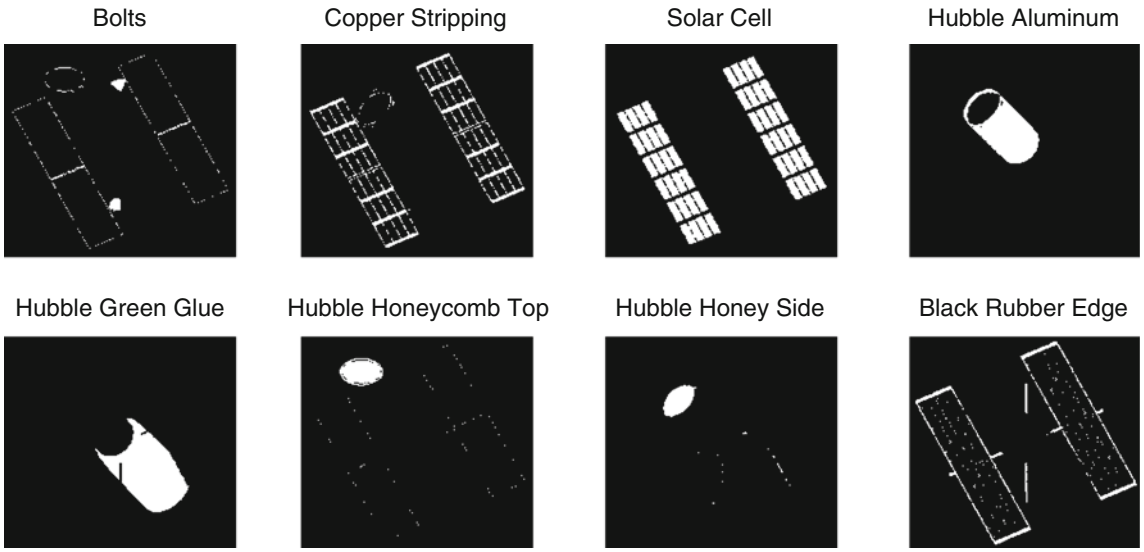

Fig. 3 The abundance maps of eight endmembers designed in the pure simulated data (the first data)

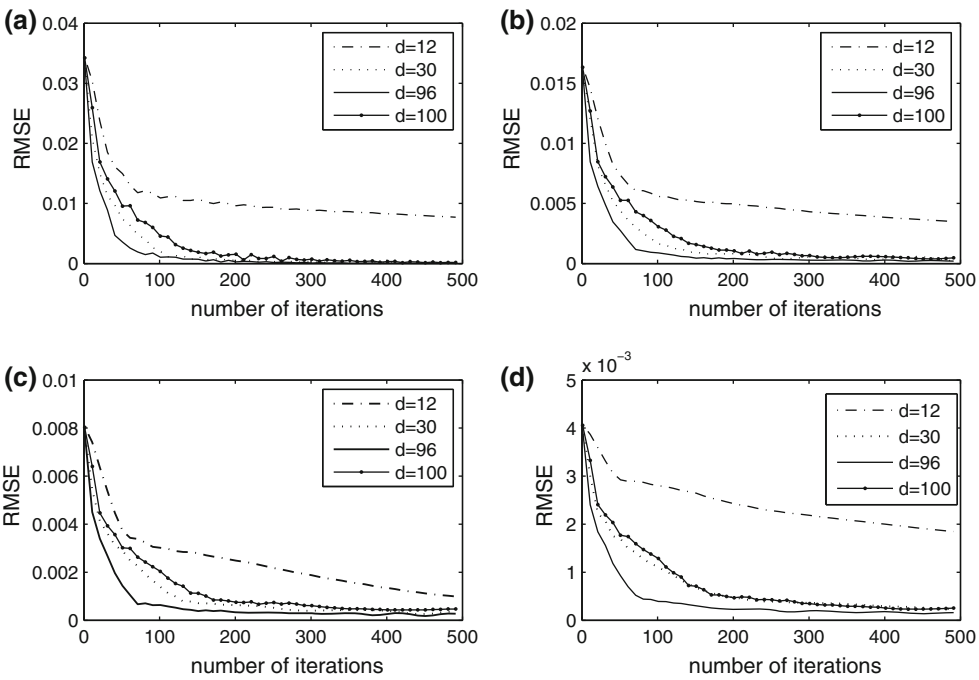

Fig. 4 The RMSE curves each maps represent different simulated hyperspectral images. (The $d = 100$ curve is the result of sparse unmixing algorithm without random projection. The other curves are the results of sparse unmixing algorithm with random projection)

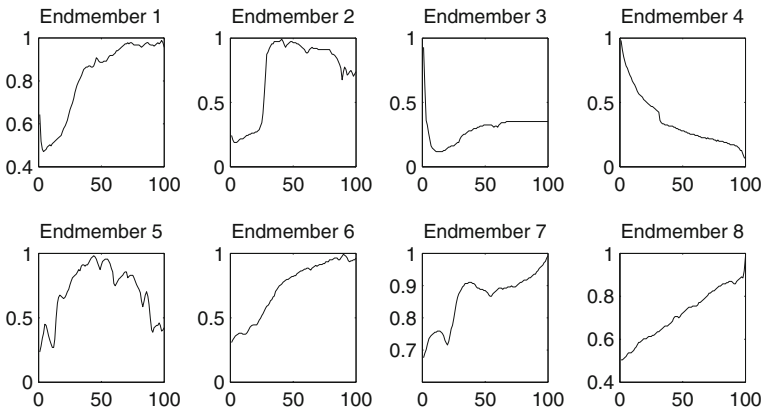

Fig. 5 The unmixed endmembers of four simulated data

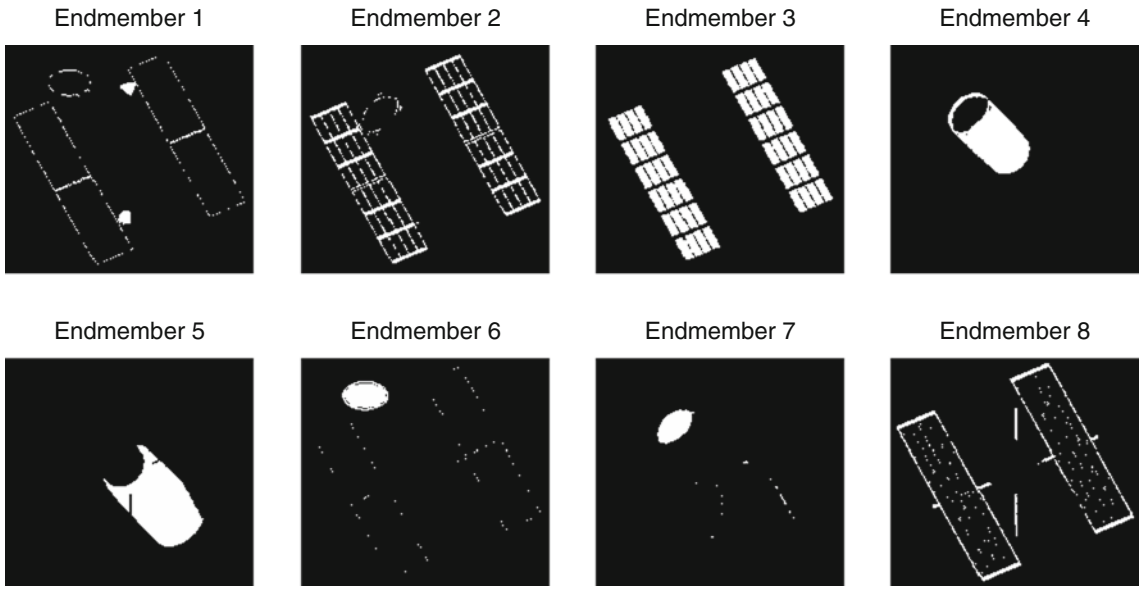

Fig. 6 The unmixed abundance maps of the first simulated data

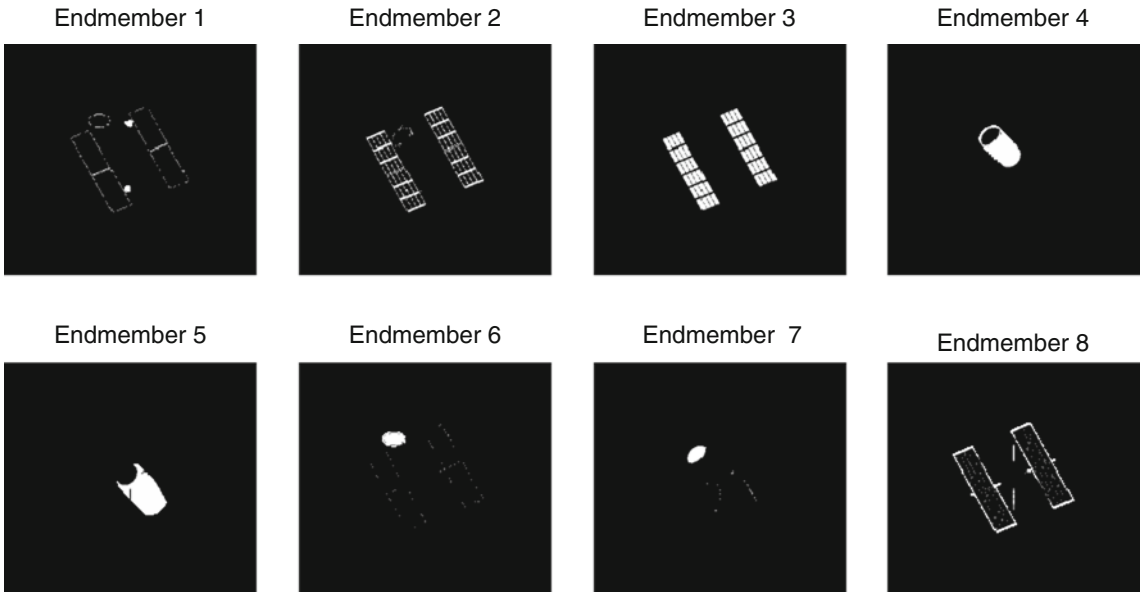

Fig. 7 The unmixed abundance maps of the second simulated data

advance, it was more efficient to evaluate the performance of many algorithms using the simulated data than using the real data. For the simulated data, the algorithms are measured by the computing time, RMSE (root mean square error) and AMSA (average minimum spectral angle). For the real data, it was hard to obtain the ground-truth maps. Therefore, we present the different solutions of the above algorithms in a straight way.

To assess the accuracy of unmixing results, we use the RMSE to estimate the deviation between the designed abundances and estimated value, defined as follows:

$$\mathrm{RMSE} = \sqrt{\frac{\sum_{i=1}^{Q}\sum_{j=1}^{K}(H_{ij} - \hat{H}_{ij})^2}{Q \times K}} \tag{19}$$

where H_{ij} is the designed abundances and $\hat{H}_{ij}$ is the estimation.

It is a good choice to measure the similarity between two spectra vectors by the spectral angle. Because the number of unmixing endmembers might not be consistent with the designed one, we adopt the AMSA to estimate the precision of endmember extraction. The AMSA defined by the following equation:

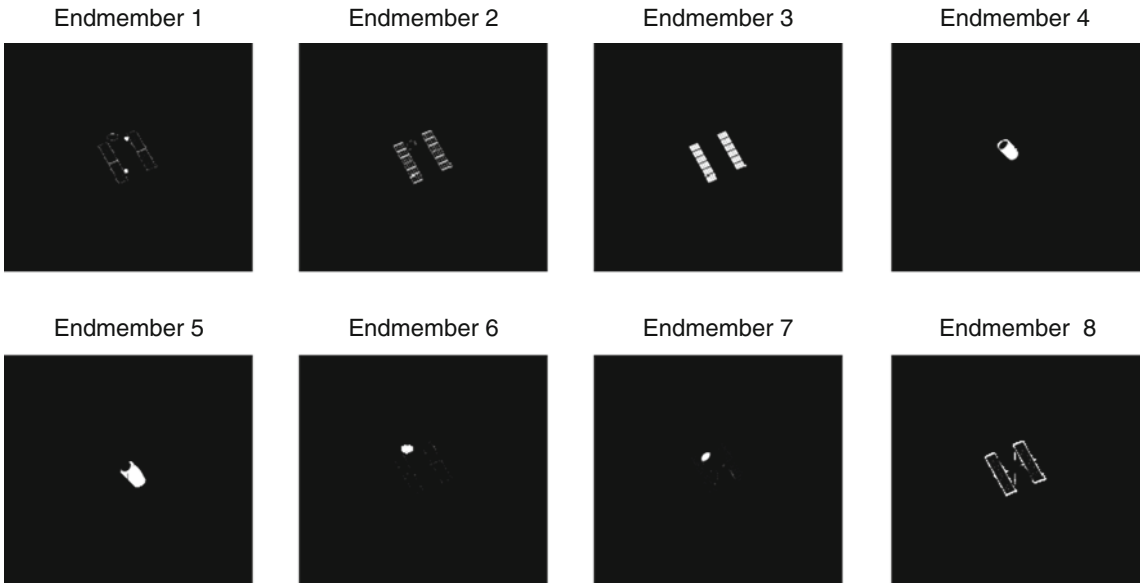

Fig. 8 The unmixed abundance maps of the third simulated data

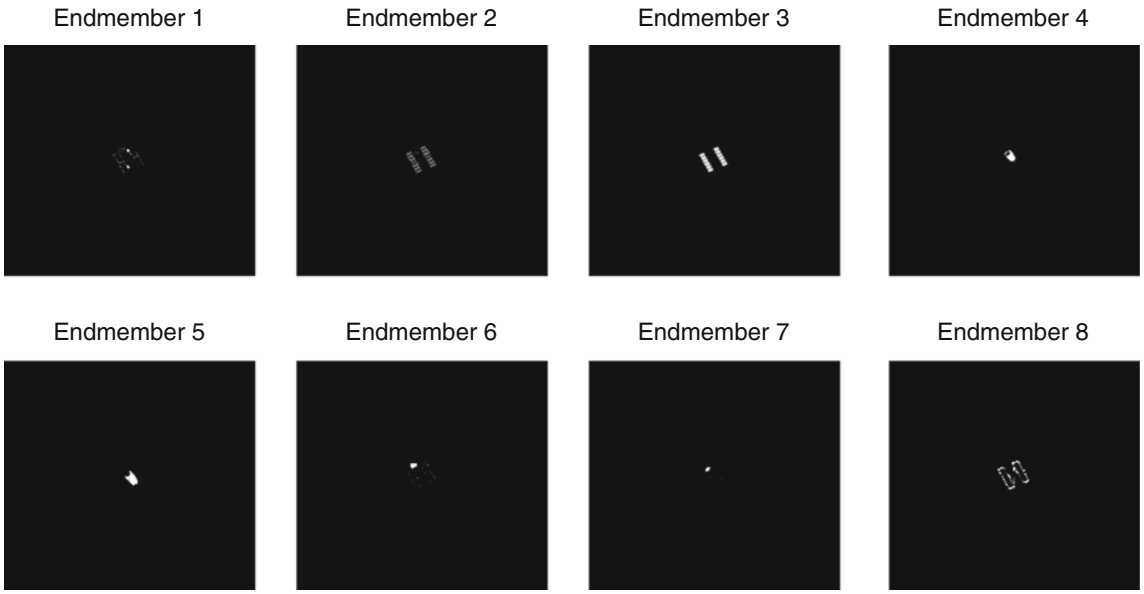

Fig. 9 The unmixed abundance maps of the fourth simulated data

Table 1 Objective indices of the SUARP and SB

		Data 1	Data 2	Data 3	Data 4
SUARP ($d = 30$)	RMSE	7.86e-005	2.93e-004	3.77e-004	2.40e-004
	AMSA	0	0	0	0
	Time consuming (s)	864.6	828.4	858.7	863.1
SB ($d = 100$)	RMSE	1.35e-004	4.88e-004	4.57e-004	2.61e-004
	AMSA	0	0	0	0
	Time consuming (s)	1317.1	1006.3	1003.9	1005.8

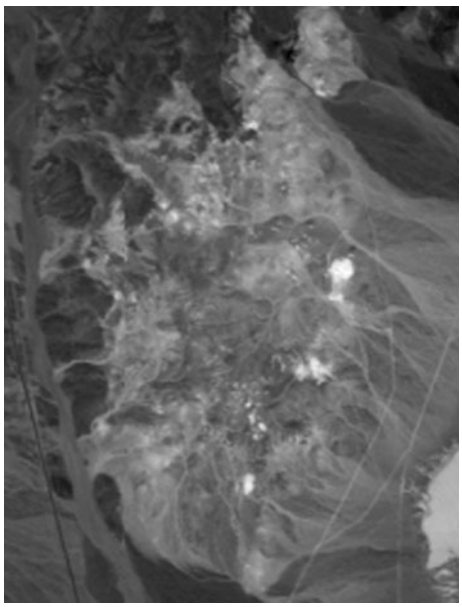

Fig. 10 Band 80 of a subimage of the AVIRIS Cuprite Nevada data

$$\text{AMSA} = \frac{1}{n}\sum_{j=1}^{n} \min_{i=1,\ldots,m} \left(\arccos \frac{\langle e_i, \hat{e}_j \rangle}{\|e_i\|_2 \cdot \|\hat{e}_j\|_2} \right) \tag{20}$$

where $\{e_1, e_2, \ldots, e_m\}$ and $\{\hat{e}_1, \hat{e}_2, \ldots, \hat{e}_n\}$ are the designed and estimated endmembers, respectively. m and n are the total numbers of the designed and estimated endmembers, respectively.

5.1 Simulated data experiment

For our numerical tests, we use the data developed by Zhang et al. [18], where the authors constructed a dataset of simulated data using a 3D model of Hubble Space Telescope and NASA library of material spectral signatures. The tested four simulated hyperspectral images have different space resolutions whose 1th band images are showed in Fig. 1. The first simulated data showed in Fig. 1a contain only pure pixels. Lowering the space resolution, the other three simulated data showed in Fig. 1b–d are mixed in a different extent. The fourth simulated data are highly mixed, which challenge the sparse unmixing algorithm. The simulated hyperspectral images consist of 8 pure spectral signatures (showed in Fig. 2) which are assigned based on orientation of the Hubble telescope. They are bolts, copper stripping, solar cell, Hubble Aluminum, Hubble green glue, Hubble honeycomb top, Hubble honeycomb side and black rubber edge, respectively. Their spectrums cover a band of spectrum from 0.4 to 2.5 μm for 100 evenly distributed sampling points, leading to a hyperspectral data of size $193 \times 177 \times 100$. Their corresponding abundance maps of the pure pixel simulated data 1 are showed in Fig. 3. The spectral library matrix S used in experiments was generated from USGS [19] digital spectral library. We select 358 typical materials' spectra with 224 spectral bands distributed uniformly in the interval 0.4–2.5 μm. Here we resample the spectra and decrease spectral bands checking with spectrums of 8 component materials. Then spectral matrix S is 100×366 size. We run our algorithm with Matlab 7.10.0 (R2010a) in the computer with $3G$ memory and 2.66 GHz frequency.

We test our sparse unmixing algorithm with four simulated hyperspectral images. Here we set $\lambda = 0.016$, $\mu = 0.05$, $\eta = 0.001$ and set the projected dimension $d = 12, 18, \ldots, 96$. As $d = 100$, it means the sparse unmixing process without random projection technique. In order to

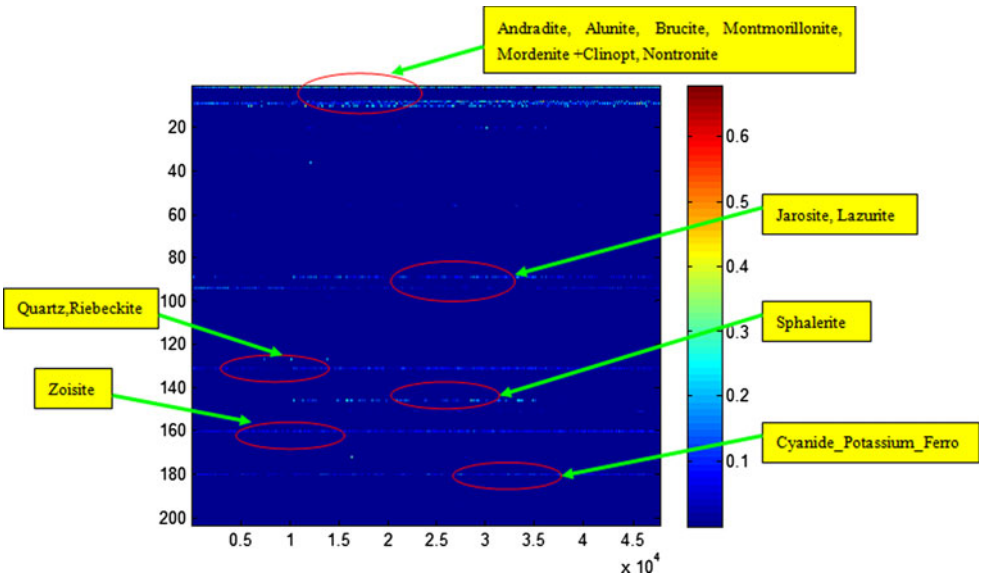

Fig. 11 Fractional abundance estimation of each spectrums in the spectral library by the SUARP. The most significant materials selected by this algorithm are outlined

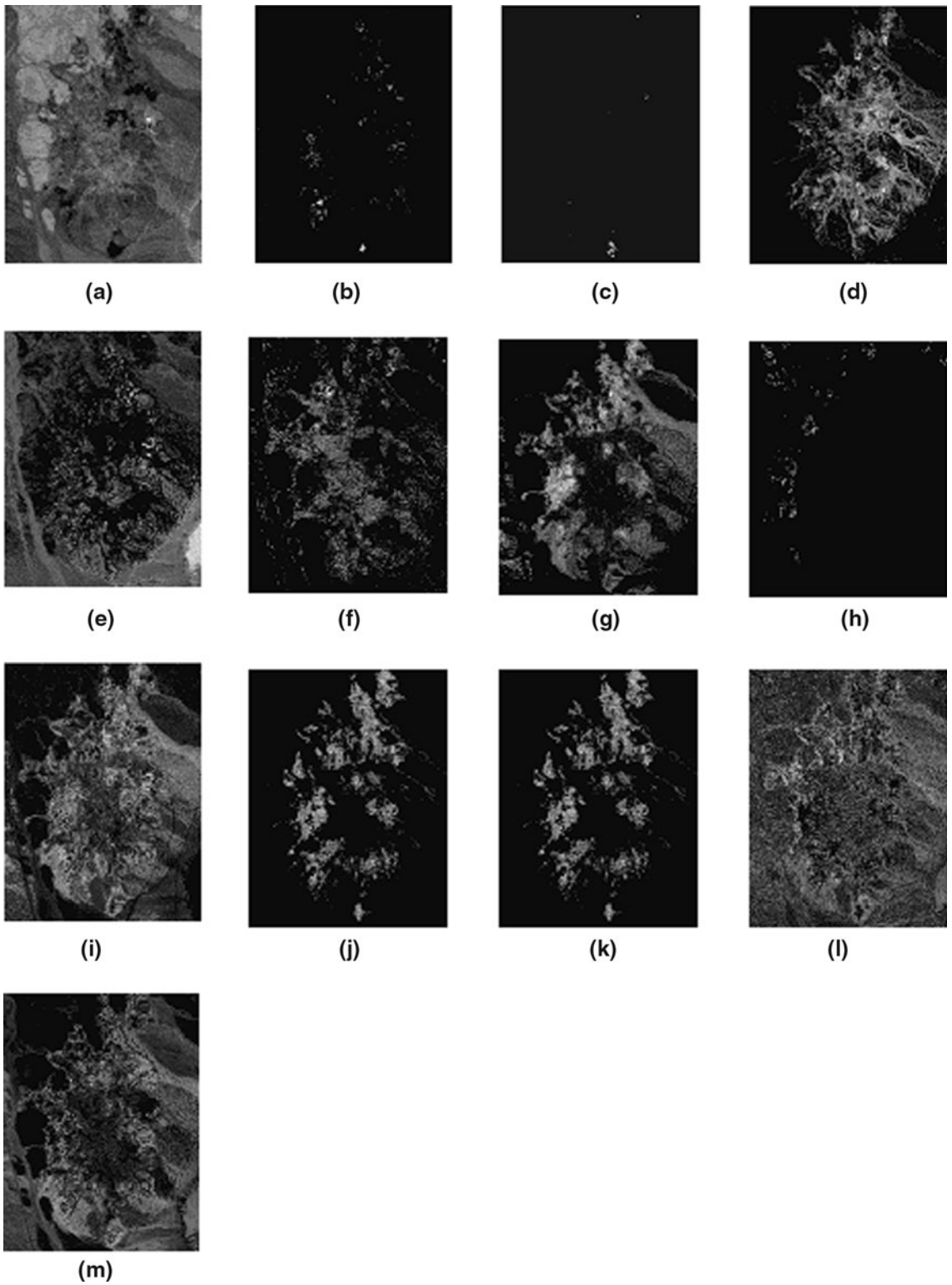

Fig. 12 Fractional abundance maps of each endmember by the SUARP, **a** andradite, **b** Alunite, **c** Brucite, **d** Montmorillonite, **e** mordenite + clinopt, **f** nontronite, **g** jarosite, **h** lazurite, **i** quartz, **j** riebeckite, **k** sphalerite, **l** Zoisite, **m** cyanide_potassium_ferro

show the efficiency of random projection, we chose $d = 123, 096, 100$ as typical representation. Figure 4 shows the variations of RMSE with respect to the number of iteration steps and the projected dimensions. The algorithm with random projection converges faster than the algorithm without random projection when the compressed

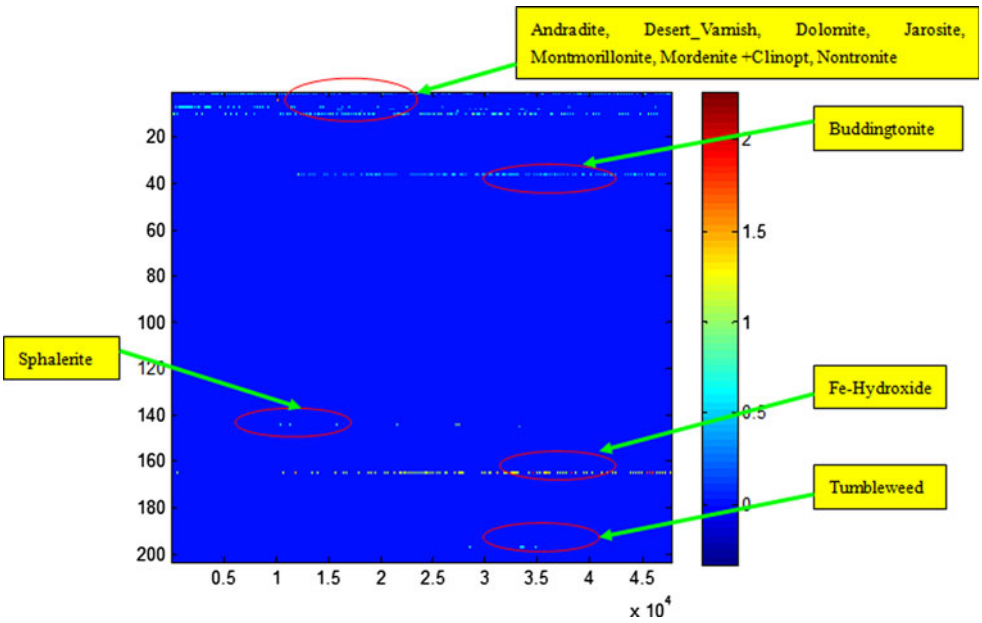

Fig. 13 Fractional abundance estimation of each spectrum in the spectral library by the OMP. The most significant materials selected by this algorithm are outlined

dimension is more than 30. It means we could set the projected dimension 30 to save the computing time. The objective indexes about RMSE, AMSA and consuming time are presented in Table 1. It demonstrates that the algorithm with random projection has a higher unmixing accuracy and works better on both the pure data and mixed data than the one without random projection, and it saves abut 10 % of the computing time than the latter one. Figure 5 shows the unmixed endmembers extracted from the spectral library and illustrates that they are the same as the designed ones comparing with Figs. 6, 7, 8 and 9 and which illustrate intuitively the corresponding abundance maps of endmembers in the unmixing results of four simulated data, respectively.

In Table 2, we evaluated the OMP, SUARP and BP quantitatively by unmixing the fourth simulated data. It demonstrates that the proposed algorithm has the most accurate result, although the consuming time is the longest. Both the OMP and BP algorithms select other spectrums from the library as endmembers, excluding the right ones. The OMP algorithm has the worst result which contains negative fractional abundances.

5.2 Real data experiment

We present the results of our methods and other classical methods of the real-world data, which is an image acquired by the airborne visible/infrared imaging spectrometer (AVIRIS) sensor over Cuprite in Southern Nevada [20]. In recent years, the Cuprite data set has been widely used for hyperspectral unmixing research [21]. Figure 10 shows the 80th band as a subimage of the original data with size 250 × 190. For our experiments, we have removed low SNR and water–vapor absorption bands (1–2, 104–113, 148–167, and 221–224), which yields 188 bands out of the original 224 bands. The Cuprite site is well understood mineralogically and has several exposed minerals of interest, all included in the USGS library considered in experiments, denoted splib06. It is worth mentioning that variants of the same mineral with slightly different spectra can be considered as the same endmember. We obtained 203 materials from the library as input to test the algorithms.

We compared the SUARP algorithm with the OMP and BP algorithms. Figures 11, 13 and 15 show that they have 13, 11 and 5 endmembers, respectively. Figures 12, 14 and 16 show their fractional abundance maps of each endmembers. They all detect the mordenite + clinopt mineral which is displayed in the Figs. 12e, 14f and 16b. Except for mordenite + clinopt mineral, the SUARP and OMP algorithms both have the andradite and montmorillonite endmembers which are showed in Figs. 12a, d and 14a, e. The SUARP and BP algorithms both have alunite and quartz endmembers which are displayed in Figs. 12b, i and 16a, d. The OMP and BP have not other same endmembers except for mordenite + clinopt mineral. It seems that the space distributions of the same endmembers are similar, but the abundances are different. The solution of BP algorithm is most sparse, but the sum of the fractional abundances of all spectrums in the spectral library is far below 1. It means there should be other endmembers which the BP algorithm did not select. The result of the OMP is doubted because of the fact that there are negative factional abundances in the solution. The six endmembers in the solution of SUARP are same as the ones obtained by the VCA algorithm. The

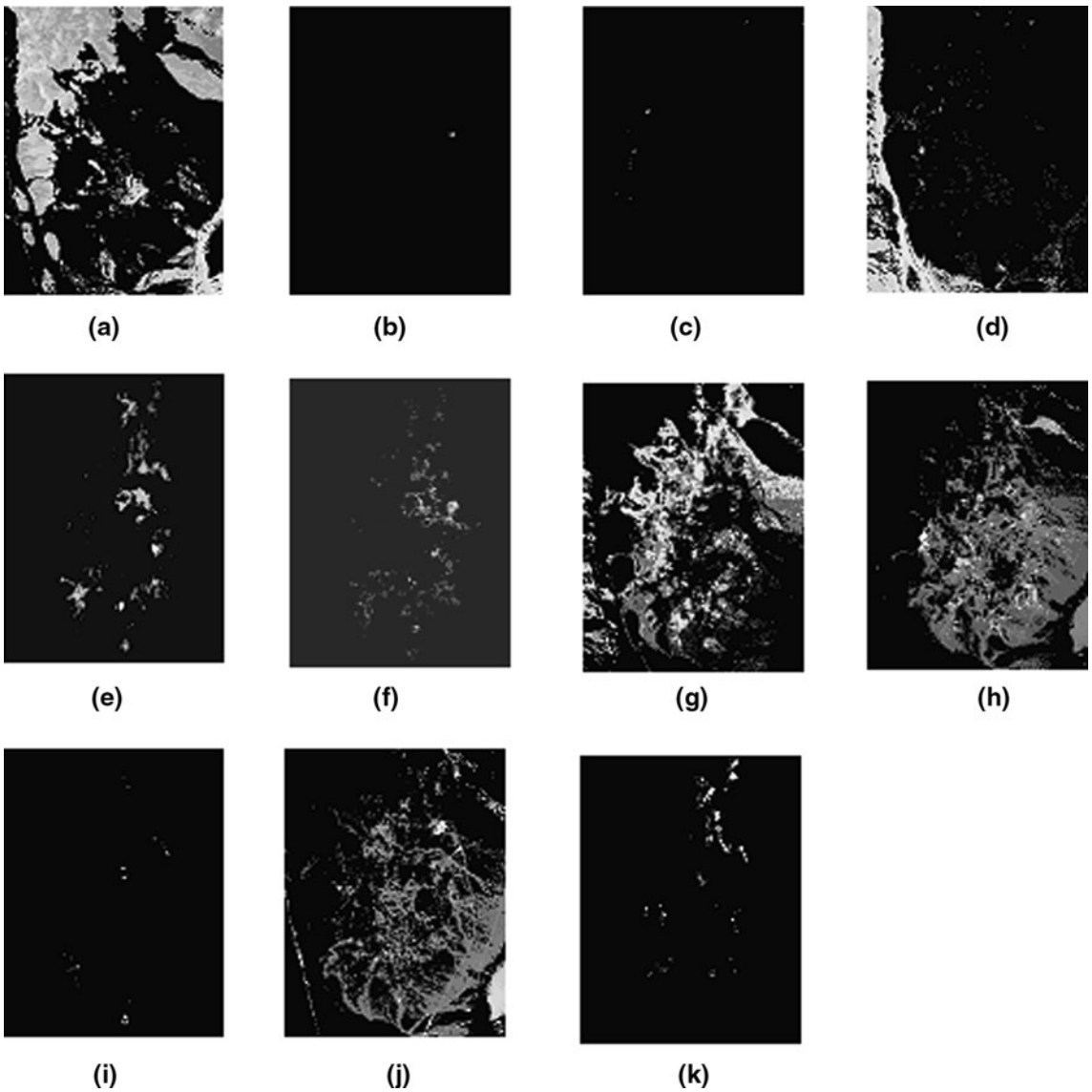

Fig. 14 Fractional abundance maps of each endmember by the OMP, **a** andradite, **b** desert_varnish, **c** dolomite, **d** jarosite, **e** montmorillonite, **f** mordenite + clinopt, **g** nontronite, **h** buddingtonite, **i** sphalerite, **j** Fe-hydroxide, **k** tumbleweed

fact illustrates the SUARP algorithm is efficient to process the real data. Table 3 shows that the OMP algorithm also computes fastest and the SUARP is faster than the BP.

The experimental results show our algorithms work well on both the simulated data and real-world data. It could identify the correct endmembers in the spectral library and estimate the abundances accurately with less computing consuming.

6 Conclusions

In this paper, we present an efficient semi-supervised unmixing method for the hyperspectral imagery. Using a large spectral database, it is an approach to solve the problem of correct endmember identification. We propose a sparse unmixing model expressed in the form of matrixes. To accelerate the sparse unmixing process, we apply random projection technique to lower the dimensions of hyperspectral images and split Bregman iteration to optimize the sparse regression problem. We give a proposal to set a fit compressed dimension by the RMSE curves. We have illustrated the utility of our unmixing method on synthetic simulated data and real-world data and compared our method to a number of alternatives. In our experiments, the result shows that the algorithm works efficiently in the endmember extraction and abundance estimation.

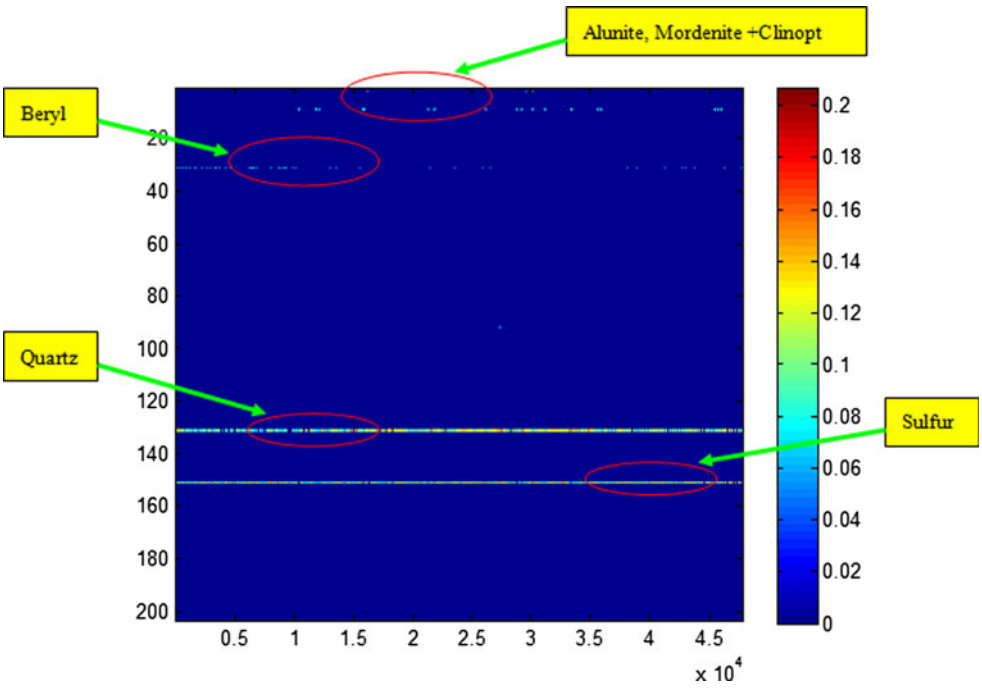

Fig. 15 Fractional abundance estimation of each spectrum in the spectral library by the BP. The most significant materials selected by this algorithm are outlined

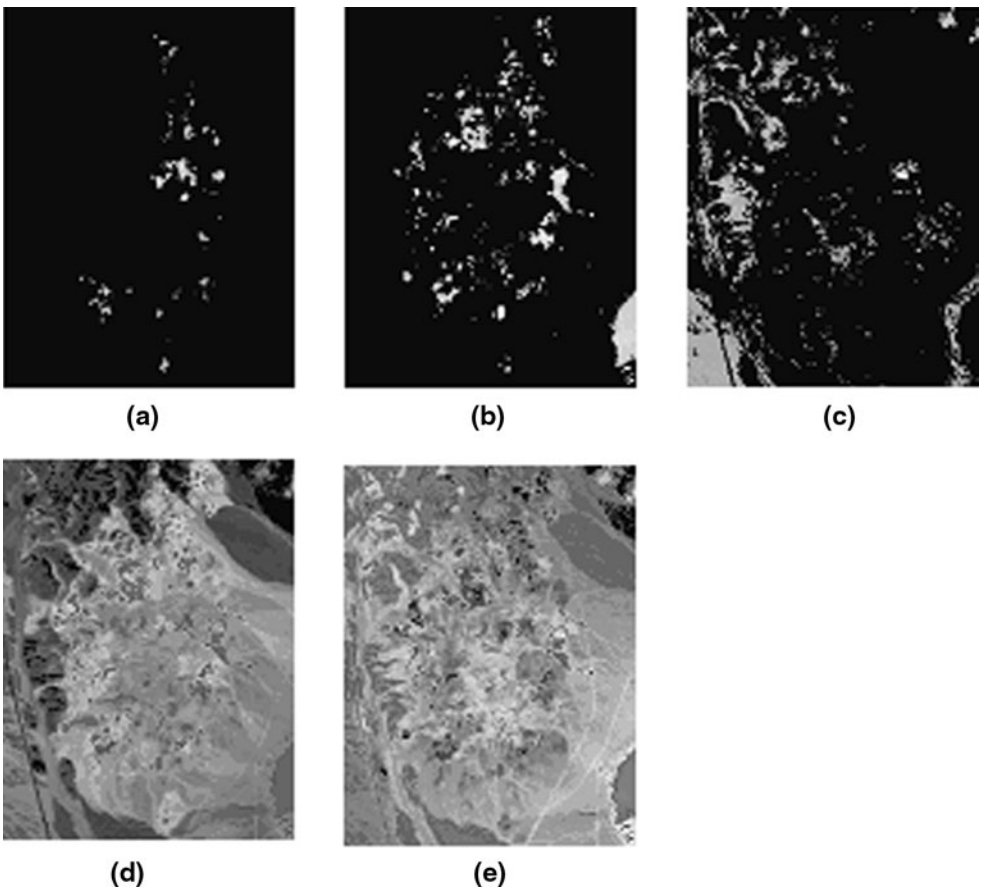

Fig. 16 Fractional abundance maps of each endmember by the BP, **a** alunite, **b** mordenite + clinopt, **c** beryl, **d** quartz, **e** sulfur

Table 2 Objective indices of the SUARP, OMP and BP

	OMP	SUARP	BP
RMSE	5.1432	1.8405e-004	0.0014
AMSA	0.0112	0	0.0082
Time consuming (s)	27.0612	594.0403	55.4379

Table 3 Time consuming of real-world data by the SUARP, OMP and BP

	OMP	SUARP	BP
Time consuming (sec)	298.3275	510.8561	5.6670e+03

Acknowledgments The work was supported by the National Natural Science Foundation of China under the Grants 61273245, 60975003 and 91120301, the 973 Program under the Grant 2010CB327904, the open funding project of State Key Laboratory of Virtual Reality Technology and Systems, Beihang University (Grant No. BUAA-VR-12KF-07), the Beijing Natural Science Foundation (Non-negative Component Analysis for Hyperspectral Imagery Unmixing) under the Grant 4112036, and Program for New Century Excellent Talents in University of Ministry of Education of China under the Grant NCET-11-0775.

References

1. Adams JB, Smith MO, Johnson PE (1986) Spectral mixture modeling: a new analysis of rock and soil types at the Viking Lander 1 site. J Geophys Res 91: 8098–8112
2. Bioucas-Dias JM, Plaza A (2010) Hyperspectral unmixing: geometrical, statistical, and sparse regression-based approaches. In: Proceedings of SPIE international society for optical engineering V, 7830
3. Boardman JW, Kruse FA, Green RO (1995) Mapping target signatures via partial unmixing of AVIRIS data. In: Proceedings of JPL airborne earth science workshop, pp 23–26
4. Winter ME (2003) N-FINDR: an algorithm for fast autonomous spectral endmember determination in hyperspectral data. In: Proceedings of SPIE image spectrometry V, 3753: 266–277
5. Ren H, Chang C-I (2003) Automatic spectral target recognition in hyperspectral imagery. IEEE Trans Aerosp Electron Syst 9(4): 1232–1249
6. Nascimento JMP, Bioucas-Dias JM (2005) Vertex component analysis: a fast algorithm to unmix hyperspectral data. IEEE Trans Geosci Remote Sens 43(4): 898–910
7. Iordache M-D, Bioucas-Dias JM, Plaza A (2011) Sparse unmixing of hyperspectral data. IEEE Trans Geosci Remote Sens 49(6): 2014–2039
8. Chan TH, Chi CY, Huang YM, Ma WK (2009) A convex analysis-based minimum-volume enclosing simplex algorithm for hyperspectral unmixing. IEEE Trans Geosci Remote Sens 47(11): 4418–4432
9. Chen J, Jia X, Yang W, Matsushita B (2009) Generalization of subpixel analysis for hyperspectral data with flexibility in spectral similarity measures. IEEE Trans Geosci Remote Sens 47(7): 2165–2171
10. Vempala S (2004) The random projection method. American Mathematical Society, Providence
11. Achlioptas D (2003) Database-friendly random projections: Johnson–Lindenstrauss with binary coins. J Comput Syst Sci 66(4): 671–687
12. Newman MEJ (2005) Power laws, pareto distributions and zipf's law. Contemp Phys 46(5): 232–351
13. Achlioptas D, McSherry F, Scholkopf B (2001) Sampling techniques for kernel methods. In: Proceedings of NIPS, pp 335–342
14. Arriaga R, Vempala S (1999) An algorithmic theory of learning: robust concepts and random projection. In: Proceedings of FOCS (also to appear in machine learning), pp 616–623
15. Goldstein T, Osher S (2009) The split Bregman method for l1 regularized problems. SIAM J Imaging Sci 2(2):323–343
16. Pati YC, Rezahfar R, Krishnaprasad P (2003) Orthogonal matching pursuit: recursive function approximation with applications to wavelet decomposition. In: Proceedings of the 27th annual asilomar conference on signals, systems and computers, Los Alamitos
17. Chen S, Donoho D, Saunders M (2001) Atomic decomposition by basis pursuit. SIAM Rev 43(1): 129C159
18. Zhang Q, Wang H, Plemmons R, Pauca P (2008) Tensor methods for hyperspectral data analysis: a space object material identification study. J Opt Soc Am A 25(12): 3001–3012
19. http://speclab.cr.usgs.gov/spectral-lib.html
20. Swayze GA, Clark RL, Sutley S, Gallagher AJ (1992) Groundtruthing AVIRIS mineral mapping at cuprite, nevada. In: Summaries of the 3rd annual JPL airborne geoscience workshop, vol 1, pp 47–49
21. Miao LD, Qi HR (2007) Endmember extraction from highly matrix data using minimum volume constrained nonnegative matrix factorization. IEEE Trans Geosci Remote Sens 45(3): 765–777